

Article

Ce₂O₃/BiVO₄ Embedded in rGO as Photocatalyst for the Degradation of Methyl Orange under Visible Light Irradiation

Damian C. Onwudiwe ^{1,2,*} , Boitumelo M. Phadi ^{1,2} and Opeyemi A. Oyewo ³ 

¹ Material Science Innovation and Modelling (MaSIM) Research Focus Area, Faculty of Agriculture, Science and Technology, North-West University (Mafikeng Campus), Private Bag X2046, Mmabatho 2735, South Africa; boitumelomosa96@gmail.com

² Department of Chemistry, School of Physical and Chemical Sciences, Faculty of Natural and Agricultural Science, North-West University (Mafikeng Campus), Private Bag X2046, Mmabatho 2735, South Africa

³ Department of Science and Technology education, University of Johannesburg, P.O. Box 524, Auckland Park 2006, South Africa; atiba.opeyemi@gmail.com

* Correspondence: Damian.Onwudiwe@nwu.ac.za; Tel.: +27-18-389-2545; Fax: +27-18-389-2420

Abstract: A p–n heterojunction semiconductor structure composed of Ce₃O₄ and BiVO₄ has been synthesized and then incorporated into reduced graphene oxide (rGO) by the hydrothermal method. The ternary composites were characterized by X-ray diffraction, transmission electron microscopy (TEM), scanning electron microscopy (SEM), electron diffraction spectroscopy (EDS), and UV–vis spectroscopy. The efficiency of the composites as photocatalysts was determined by studying the oxidative degradation of methyl orange in aqueous solution under visible light irradiation. The effect of parameters such as pH, catalyst loading, and concentration of the dye solution was examined in order to determine their influence on the photocatalytic activity of the composites. The composite incorporated into reduced graphene oxide presented the highest percentage (above 90%) in 2 h time, attributed to the effect of the increased surface area. The process of the enhanced photocatalytic activity has been discussed based on the energy band positions of the nanoparticles within the composite.

Keywords: Ce₂O₃/BiVO₄ photocatalyst; p–n heterojunction; reduced GO; photocatalysis; visible light; dye degradation



Citation: Onwudiwe, D.C.; Phadi, B.M.; Oyewo, O.A. Ce₂O₃/BiVO₄ Embedded in rGO as Photocatalyst for the Degradation of Methyl Orange under Visible Light Irradiation. *J* **2021**, *4*, 154–168. <https://doi.org/10.3390/j4020013>

Academic Editors: Salvatore Scire` and Roberto Fiorenza

Received: 15 April 2021
Accepted: 31 May 2021
Published: 7 June 2021

Publisher's Note: MDPI stays neutral with regard to jurisdictional claims in published maps and institutional affiliations.



Copyright: © 2021 by the authors. Licensee MDPI, Basel, Switzerland. This article is an open access article distributed under the terms and conditions of the Creative Commons Attribution (CC BY) license (<https://creativecommons.org/licenses/by/4.0/>).

1. Introduction

Bismuth vanadate (BiVO₄) is a ternary, non-toxic, n-type semiconductor oxide with a layered structure. It has drawn a lot of attention due to its nontoxic nature, low cost, and unique properties such as ionic conductivity, ferro-elasticity, light harvesting capacity, and high stability. These are responsible for its potential application in different areas such as electronic devices, gas sensing, pigment industries, and in the photocatalytic decomposition of organic pollutants [1]. It is currently considered as one of the significant photocatalysts that utilizes visible light because of its narrow band gap of 2.4 eV. However, it is one of the metal oxides, in which the fast recombination rate of the photo-generated electron-hole pairs still hinders its photocatalytic activity [2].

Recently, attention has been focused on the combination of two types of semiconductors to form a heterojunction system as one of the strategies used to address the challenges associated with the large band gap and rapid recombination of the photo-generated charge carriers in most semiconductors [3,4]. Contrary to a single phase photocatalyst, the formation of heterojunction semiconductors or multi-semiconducting materials has been reported to attain significant enhancements in the promotion of electron-hole pairs separation. This results in the preservation of oxidation-reduction reactions at the conduction and valence band positions [5,6]. The effective transfer of electron-hole from one semiconductor material to another, with the suitable band edge position, could reduce the fast

recombination of the photo-induced electron-hole pairs significantly, thereby resulting in an upsurge of the charge carrier's lifetime and consequently promoting the efficacy of the photocatalytic process [7,8]. Different types of heterojunctions of bismuth vanadate have been reported for various applications. For example, Sitaaraman et al. [9] fabricated a heterojunction BiVO₄ and WO₃ for solar water splitting applications. BiVO₄/BiOx heterojunction has been reported for enhanced photo-electrochemical performance [10]. An enhanced photocatalytic activity was achieved using tungsten-doped BiVO₄/WO₃ heterojunction materials [11]. The visible-light-driven photocatalytic synthesis of imines has been reported using BiVO₄/g-C₃N₄ [12]. Different bismuth-based oxides have also been composited with other semiconductors to form heterojunctions such as Bi₂O₂CO₃/Bi₄O₇ [13] and g-C₃N₄/Bi₄O₇ [14], including ternary heterojunctions like Ag/Bi₄O₇/g-C₃N₄ [15] and Bi₂O₄-Bi₄O₇-BiO_{2-x} [16], which demonstrated outstanding activities.

To form a heterojunction system, metal oxide semiconductors are usually preferred due to their chemical stability, easy availability, and favourable band gaps [9]. Many of them also have good light-induced properties, making them suitable combinations for photocatalytic processes. Cerium oxide is a rare earth metal with unique properties and is commonly used as a support for catalytically active materials due to its electronic property and redox behavior. It has high surface to volume ratio and quantum size effect at nanoscale, which improves the interfacial activity. It shows good optical and photocatalytic properties, has a wide band gap of 3.2 eV that contributes to its ability to absorb UV, and has high thermal stability [17]. It has been used in different applications such as catalysis, fuel cells, gas sensors and optical devices [18]. The p-type Ce₂O₃ is suitable to combine with the n-type BiVO₄ for the formation of p-n heterojunction and also for the acceleration of charge transfer for photocatalytic processes, specifically in the degradation of dyes. In order to improve the surface area of semiconductor and enhance the interaction of dye molecules with the photocatalyst, one of the most common approaches is the incorporation of polymeric material such as graphene oxide.

Graphene oxide is a zero band gap semiconductor resulting in excellent properties such as high thermal stability, high heat conductivity, large surface area, high mechanical toughness, and good optical transparency. The chemical configuration of GO, which has a sp³ carbon domain adjoining sp² carbon, with functional groups such as carboxyl, hydroxyl, and epoxy gives rise to the incredible characteristics of this interesting material [19]. It has been used to support nanomaterials to make nanocomposites due to its exceptional properties and good biocompatibility. It has a larger surface area than other carbon materials. The larger surface area enhances contact with compounds, and thereby reduces the agglomeration of the nanoparticles. In addition, the existence of inorganic nanoparticles on the surfaces of the graphene sheets prevents the aggregation of graphene sheets during reduction. This helps to keep the specific surface area of the resultant composite materials very large, an important property required for adsorption and subsequent photocatalytic degradation of pollutants [20,21]. Graphene oxide has good adsorption property [22], and its use for nanocomposite formation improves degradation of organic pollutants, via the reduction of the rate of recombination, and improvement of light absorption and promotion of charge carrier migration. The number of electron-hole pairs formed in the redox reaction that occurs during photocatalysis relies on the active sites that are on the surface of the photocatalyst. To increase the performance of the photocatalyst, the active sites are important. In this study, GO has been used as substrate to increase electrocatalytic sites in the nanocomposites (Ce₂O₃-BiVO₄), and also to act as the adsorption sites for the dye molecules.

Dyes are one of the essential raw materials used in different industries such as the paper, food, plastic, and textile industries [23]. The discharge of dyes into the aquatic environment is hazardous to biodiversity [24]. Most of them are carcinogenic, interrupt the nervous system, damage organs, and interfere with DNA structure [25]. A typical example is methyl orange, which is a commonly used azo dye in textiles, pharmaceuticals, clothing, photography, and in paper industries [26]. About 50% of textile azo dyes have been

reported not to bind to fabric or paper during the dyeing process, resulting in their release into water bodies where they pose great danger to living organisms [27]. The removal of synthetic dyes from water has drawn a great attention, and different methods have been developed for this process. The limitation of most of these methods is that they cannot completely break down these dyes to form simple harmless compounds. For this reason, advanced treatment methods for dye degradation that uses nontoxic compounds are in high demand. One of these advanced methods of dye removal is photocatalysis, which makes use of semiconductor nanomaterials. Metal oxides have been widely utilized as photocatalysts and among them are bismuth vanadate and cerium oxide. In this study, we report the synthesis of $\text{Ce}_2\text{O}_3/\text{BiVO}_4$ embedded in rGO and evaluated the photocatalytic efficiency for the degradation of methyl orange under visible light irradiation

2. Materials

Bismuth nitrate pentahydrate, ammonium metavanadate, ethylene glycol, cerium nitrate hexahydrate, potassium permanganate, graphite flakes, hydrogen peroxide, sulphuric acid, phosphoric acid, and ethylene glycol were purchased from Merck or Sigma-Aldrich. They were of analytical grade and were used as received. Distilled water was used for all the solutions preparation.

2.1. Methods

2.1.1. Synthesis of Graphene Oxide

Graphene oxide was synthesised using a modified hummer's method [28]. Concentrated sulphuric acid (H_2SO_4 , 360 mL) and concentrated phosphoric acid (H_3PO_4 , 40 mL) were stirred in a beaker for 10 min. Graphite flakes (3 g) and potassium permanganate (KMnO_4 , 18 g) were mixed together in a 1000 mL beaker. Then, the solution of the acids was transferred gradually into the 1000 mL beaker of graphite and KMnO_4 . The whole mixture was stirred for 24 h at 60 °C. Thereafter, 400 mL of distilled water was added, followed by a dropwise addition of 5 mL of hydrogen peroxide until the mixture turned yellow. The suspension was allowed to stand for 1 h. Afterwards, it was centrifuged, washed with distilled water, followed by ethanol for three times until the filtrate was neutral. The product was dried in the oven for 10 h.

2.1.2. Preparation of $\text{Ce}_2\text{O}_3/\text{BiVO}_4$ Nanoparticles

About 0.4 g of $\text{Bi}(\text{NO}_3)_3 \cdot 5\text{H}_2\text{O}$ and 0.05 g of $\text{Ce}(\text{NO}_3)_3 \cdot 6\text{H}_2\text{O}$ were dissolved in 30 mL of ethylene glycol and stirred. After 30 min, a solution of 0.1 g of NH_4VO_3 in 30 mL of distilled water was added in dropwise while the constant stirring continued for another 30 min. The solution was then transferred into an autoclave and heated for 10 h at 180 °C. At the end of the reaction, the solution was allowed to cool down to room temperature and the product was washed with methanol and then dried in the air.

2.1.3. Preparation of $\text{Ce}_2\text{O}_3/\text{BiVO}_4$ in rGO

Graphene oxide solution was prepared by dispersing 1 g of the prepared graphene oxide in 10 mL of distilled water and sonicating for 2 h. Into this was added a solution of bismuth nitrate (0.4 g), cerium nitrate (0.05 g) and ammonium vanadate (0.1 g) and stirred for 30 min. The ternary solution was transferred to an autoclave, heated up to 180 °C and maintained for 10 h. Afterwards, the product was collected, centrifuged and the solids were rinsed using methanol and air dried.

2.2. Characterizations

The crystalline structures of the nanoparticles were analysed by X-ray diffraction (XRD, Bruker Advance D-8, Karlsruhe, Germany) equipped with a proportional counter using $\text{Cu K}\alpha$ radiation ($\lambda = 1.5405 \text{ \AA}$, nickel filter). Samples were placed on a flat steel sample holder and scanned from 10 to 80 °C. The diffraction peaks were matched with other recorded standards in JCPDS. The external morphology was studied using a scanning electron

microscope (JEOL 6400F Field Emission SEM at 5 kV, by Zeiss, Oberkochen, Germany), while transmission electron microscopy (Hitachi HF-2000 TEM at 200 kV by Hitachi High-Tech Corporation, Tokyo, Japan) was used to examine the internal morphology. The optical absorption property of the nanoparticles was measured using a Varian UV-vis spectrophotometer.

3. Results and Discussion

3.1. XRD Analysis

The XRD analysis of the samples was carried out in order to determine the crystalline phases of the composites before and after the incorporation of GO. As presented in Figure 1a, the XRD pattern of the $\text{Ce}_2\text{O}_3/\text{BiVO}_4$ showed diffraction peaks at 2θ of 18.99° , 28.90° , 30.54° , 34.60° , 35.15° , 35.22° , 40.04° , 42.58° , 50.33° , 53.35° , 58.59° , and 59.64° , which were attributed to the (011), (121), (040), (200), (002), (112), (150), (042), (202), (222), (321), and (123) of the monoclinic phase of BiVO_4 (JCPDS No. 14-0688) [29]. The Ce_2O_3 peaks were identified at 32.59° , 46.64° , 56.65° , and 63.07° , ascribed to (001), (110), (021), and (202) crystalline planes, which matched with the hexagonal Ce_2O_3 structure of JCPDS No. 044-1086 [30]. The appearance of both the bismuth vanadate and cerium oxide peaks confirmed the coexistence of the two semiconductor oxides in the same system.

The $\text{Ce}_2\text{O}_3/\text{BiVO}_4/\text{rGO}$ composites showed similar diffraction peaks (Figure 1b) with the pure $\text{Ce}_2\text{O}_3/\text{BiVO}_4$ nanoparticles, but no diffraction peaks of GO were observed. This was because the regular stack of GO sheets has been destroyed by the intercalation of $\text{Ce}_2\text{O}_3/\text{BiVO}_4$ nanoparticles [31] and also due to the reduction of GO to rGO during the synthesis [32,33]. Figure 1c shows the diffraction pattern of the GO with its characteristic (002) peak identified at $2\theta = 12.5^\circ$. In Figure 1b, a diffraction peak associated with reduced graphene oxide was observed at 24° , which further confirmed the reduction of GO [34]. No characteristic peaks of other samples were observed, which means there were no impurities.

A comparison of the peak intensities of the pure $\text{Ce}_2\text{O}_3/\text{BiVO}_4$ with the GO-incorporated composite showed a decrease in intensity with the addition of GO. The low intensity of the composite could be a result of the covering of the surface of the nanoparticles ($\text{Ce}_2\text{O}_3/\text{BiVO}_4$) by graphene oxide, thereby causing a reduction in the crystallinity of the composite. The addition of GO did not alter the crystal phase of the nanoparticles but caused a decrease in the particle size as evident in the broadness of the diffraction peaks. Although low crystallinity has been reported to reduce the photocatalytic activity of particles [35], the reduction in particle size enhances the photocatalytic property of nanomaterials. Furthermore, the incorporation of GO into the photocatalyst is known to increase the surface area and stability of the photocatalyst for wastewater treatment, thus increasing the activity [36].

3.2. Morphology Studies

Figure 2 shows the typical SEM and TEM images of the prepared GO, which contains layered structure of GO with exfoliated and crumpled sheets [37,38]. This carbonaceous material is also composed of various oxygen-containing functional groups including epoxy, carbonyl, carboxyl, and hydroxyl groups. While the epoxy and hydroxyl groups are found on the main surface area of GO sheets, the functional groups such as carboxyl and carbonyl groups are located at the edge of GO sheets [39].

The surface morphology of the composites was analysed using SEM and TEM analyses. Figure 3a,b show the SEM and TEM images of the $\text{Ce}_2\text{O}_3/\text{BiVO}_4$ nanoparticles. The SEM image displayed obvious short rod-like morphology, and the TEM images showed that some of these rods were somewhat agglomerated to form elongated rods. The SEM image of the composite with GO does not show a clear presence of rGO at low magnification (Figure 3c), but a dense agglomerate of particles decorated on the surface of the rGO nano-sheet. The ratio of the nanoparticles to the rGO is a major factor in the formation of composites with rGO. The high magnification SEM image of the composite (Figure 3d) showed spherically-shaped particles distributed across the rGO sheets. From Figure 3d, it can be observed that the rGO has a crumpled and layered structure.

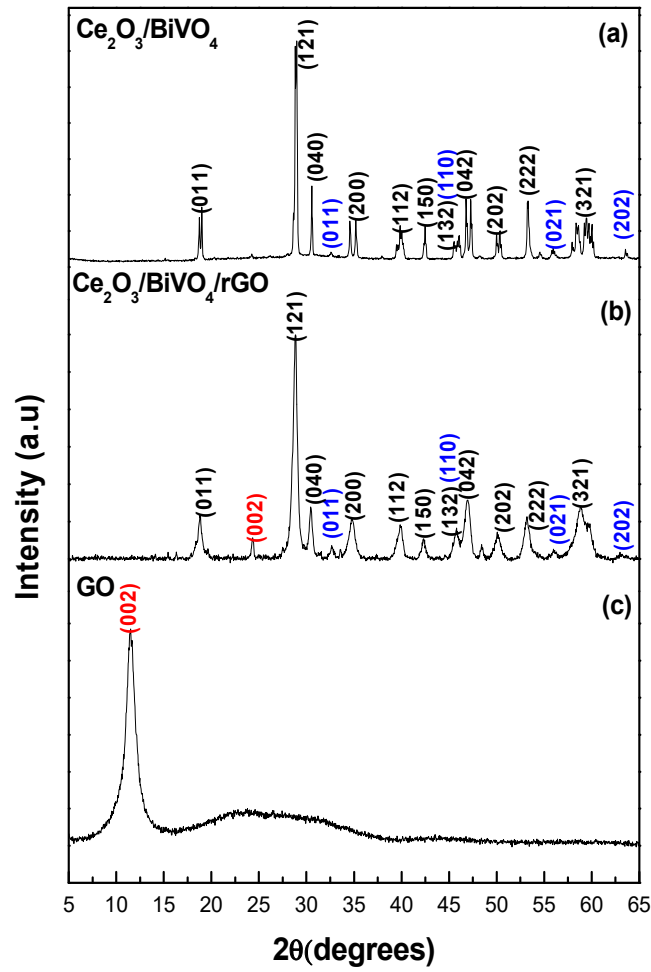


Figure 1. XRD pattern (a) $\text{Ce}_2\text{O}_3/\text{BiVO}_4$, (b) $\text{Ce}_2\text{O}_3/\text{BiVO}_4/\text{rGO}$ composite. (Black—bismuth vanadate; Red—graphene oxide; Blue—cerium oxide) and (c) graphene oxide.

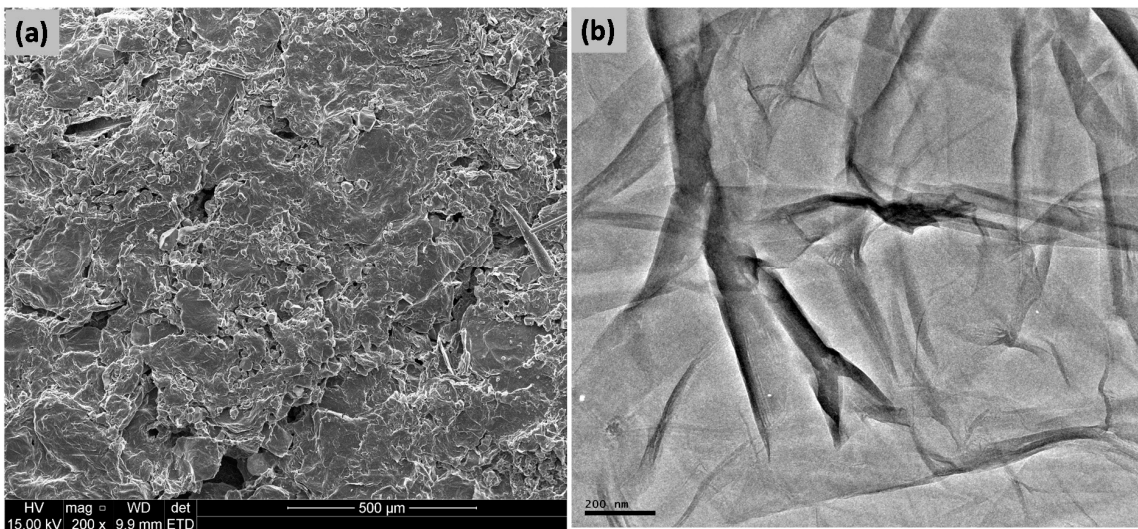


Figure 2. (a) SEM and (b) TEM micrographs of rGO.

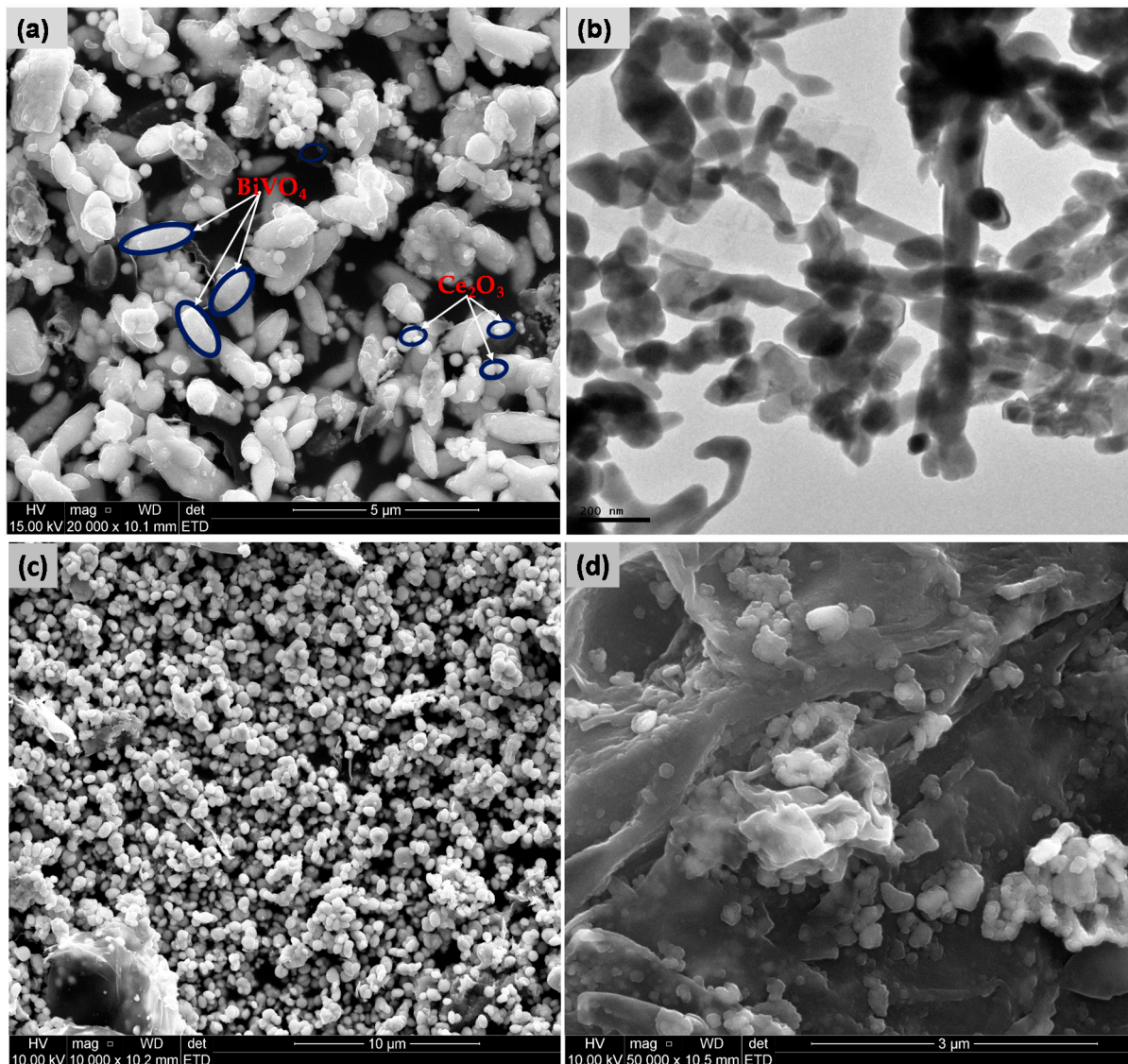


Figure 3. (a) SEM and (b) TEM micrographs of Ce₂O₃/BiVO₄; and (c) SEM and (d) TEM micrographs of Ce₂O₃/BiVO₄ incorporated into rGO.

The distribution of the Ce₂O₃/BiVO₄ nanoparticles on the surface of rGO could be ascribed to the interaction of the nanoparticles with surface functional groups on the rGO. During the solvothermal reduction process, most of the functional groups on the surface of the GO would have been reduced; however, the electrostatic and/or van der Waals forces were still enough to induce some interaction between the nanoparticles and the surface of the rGO. The adsorption process between the remaining carboxyl groups at the surface of the rGO and the nanoparticles has also been reported to be responsible for the incorporation of the nanoparticles into the reduced GO [40]. Figure 4a,b shows the EDX spectra of the Ce₂O₃/BiVO₄ nanoparticles and the composite, respectively. The spectra clearly indicated Bi, V, Ce, and O as the main constituent elements of the nanoparticles. In the composite with rGO, the additional strong C peak confirms the presence of GO and a successful loading of the nanoparticles on the GO.

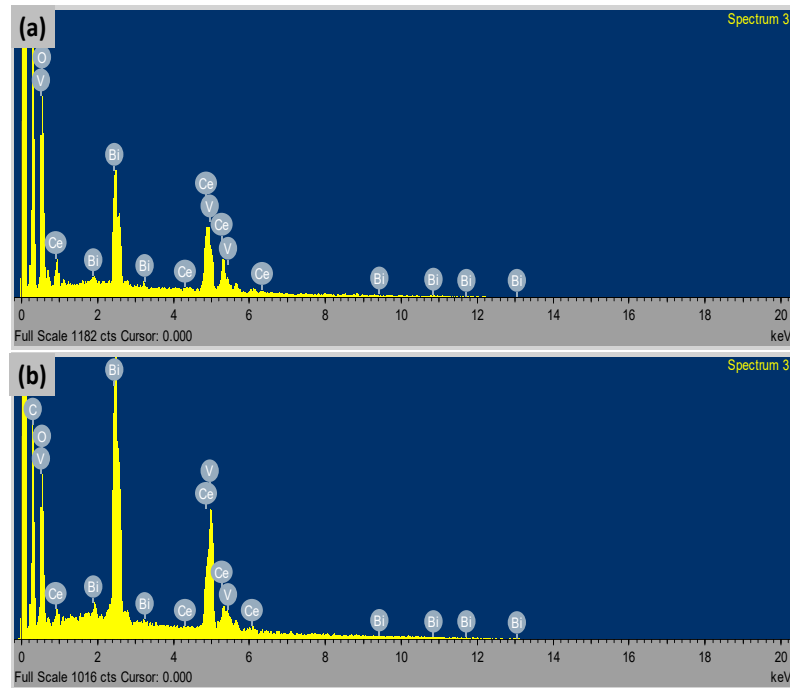


Figure 4. EDX of (a) $\text{Ce}_2\text{O}_3/\text{BiVO}_4$, and (b) $\text{Ce}_2\text{O}_3/\text{BiVO}_4$ incorporated into rGO.

3.3. FTIR Spectroscopy

Figure 5 presents the FTIR spectra of GO and $\text{Ce}_2\text{O}_3/\text{BiVO}_4/\text{rGO}$ overlapped for proper comparison. The spectrum of the GO exhibited many strong vibrational peaks, which corresponded to various oxygen functional groups. The observed peaks at 3217, 1737, 1599, 1384, 1338, and 1050 cm^{-1} were the characteristic peaks associated with hydroxyl ($-\text{OH}$), $\text{C}=\text{O}$, $\text{C}=\text{C}$, $\text{C}-\text{O}$ (carboxy), $\text{C}-\text{H}$, and $\text{C}-\text{O}$ (alkoxy) groups of GO, respectively [41]. In the spectrum of the nanocomposite, $\text{Ce}_2\text{O}_3/\text{BiVO}_4/\text{rGO}$, there are noticeable decrease in the intensity of those peaks associated with the oxygen functional groups. This indicated a reduction of GO to rGO. The $\text{M}-\text{O}-\text{C}$ bonds ($\text{M} = \text{Ce}$ or Bi), which usually appear below 900 cm^{-1} , was found around 860 cm^{-1} and indicated the interaction of the metal oxide with graphene [21,41].

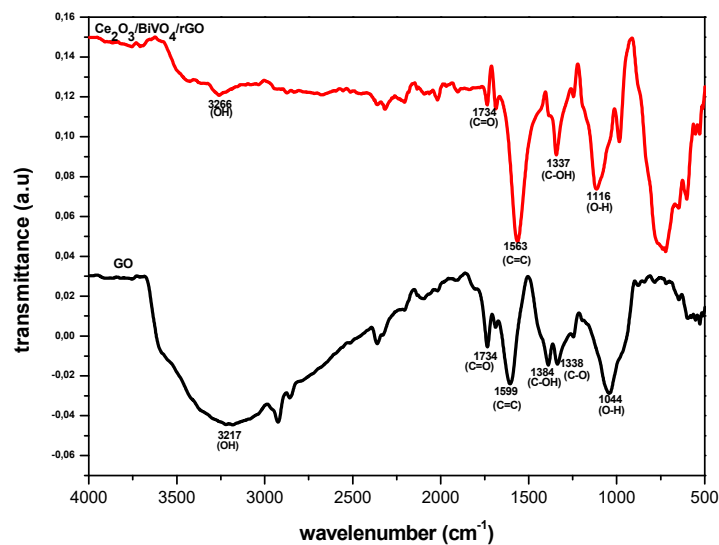


Figure 5. FTIR spectra of the synthesized GO and $\text{Ce}_2\text{O}_3/\text{BiVO}_4/\text{rGO}$.

3.4. Optical Spectroscopy

The optical property of the prepared photocatalyst was studied using UV–vis and fluorescence spectrophotometry. The qualitative analysis of semiconductor materials using UV–vis is based on the use of light in the UV and visible part of the electromagnetic spectrum to effect the excitation of electrons in either the atomic or molecular ground state to higher energy levels. This gives rise to an absorbance, which is at wavelengths that are specific to each molecule or material being analysed [42,43].

Molecules or semiconductors containing either π - or non-bonding electrons are able to absorb energy in the form of UV or visible light, which causes excitation of the electrons from lower to higher energy levels or antibonding molecular orbitals [44,45]. Some molecules or materials with easily excited electrons, for example those with low energy gaps between the lowest unoccupied molecular orbital (LUMO) and the highest occupied molecular orbital (HOMO), or between the valence band and the conduction band, could absorb light with longer wavelength in the UV–vis range of the electromagnetic spectrum [46].

The molecular structure of the material determines the absorbance of light. When the light rays pass through the material, scattering, transmittance, or absorbance could occur. The shape, size, and type of solvents used during the synthesis of the material also contribute to the optical behavior of the material. The overlapped absorption spectra of the synthesized nanoparticles and the composite with graphene oxide is shown in Figure 6a. The nanoparticles showed absorption in the UV and visible regions, with an increase in absorption intensity in the visible region upon the formation of the GO composite. The difference in the absorption intensity in the visible region suggests the formation of new material whose property is different from the prepared $\text{Ce}_2\text{O}_3/\text{BiVO}_4$. The Tauc equation was used to calculate the band gap energies of the photocatalysts, and the graphs are shown in Figure 6b,c. The values of the band gaps were 3.25 and 2.99 eV for $\text{Ce}_2\text{O}_3/\text{BiVO}_4$ and $\text{Ce}_2\text{O}_3/\text{BiVO}_4/\text{rGO}$, respectively. The relatively lower band gap energy observed for the nanocomposites involving rGO indicated a red shift in the absorption spectrum and a consequence of size increase. Furthermore, the increased band gap energy of the nanocomposite compared to the value for BiVO_4 (2.54 eV) was due to size reduction within the nanometric dimension.

3.5. Photocatalytic Activity

The photocatalytic performance of the composite was evaluated by studying the photocatalytic degradation of methyl orange under visible light irradiation. A control experiment on the degradation of the dye in the absence of the photocatalysts was also performed. Methyl orange is a common anionic dye, which contains the azo group ($-\text{N}=\text{N}-$) that connects to sp^2 -hybridized C-atoms of the aromatic group [47,48]. The absorption property is pH dependent. Thus, the UV–visible absorption spectra of the MO were first studied at different pH in order to examine the structural changes of the dye molecules and to also determine the best pH for the conduction of the photodegradation study. Figure 7a presents the absorption spectra at pH 3, 5, and 7, which showed that the maximum absorption peak shifted from 465 nm at pH 10.0 to 512 nm at pH 3.0, indicating the change in the structure of methyl orange. Obviously, the lowest degradation of methyl orange is obtained in basic or neutral media, while its highest degradation is in the acidic media. The adsorption ability of dyes changes significantly with a pH from 2.5 to 10.0. This is dependent on the nature of the dye and also determines the removal efficiency when using a photocatalyst. For example, Nguyen et al. [49] reported an increase in color removal efficiency for MB and a decrease for MO after 40 min reaction in the dark. This observation was partly ascribed to the change of surface charge of the catalyst with the pH, resulting in different degrees of repulsion force between the dye molecules and the catalysts. This influences the activity of the photocatalyst since the OH radicals at the surface of the catalyst attack the pollutant molecules harder. Consequently, there is a decrease in the rate of degradation [50].

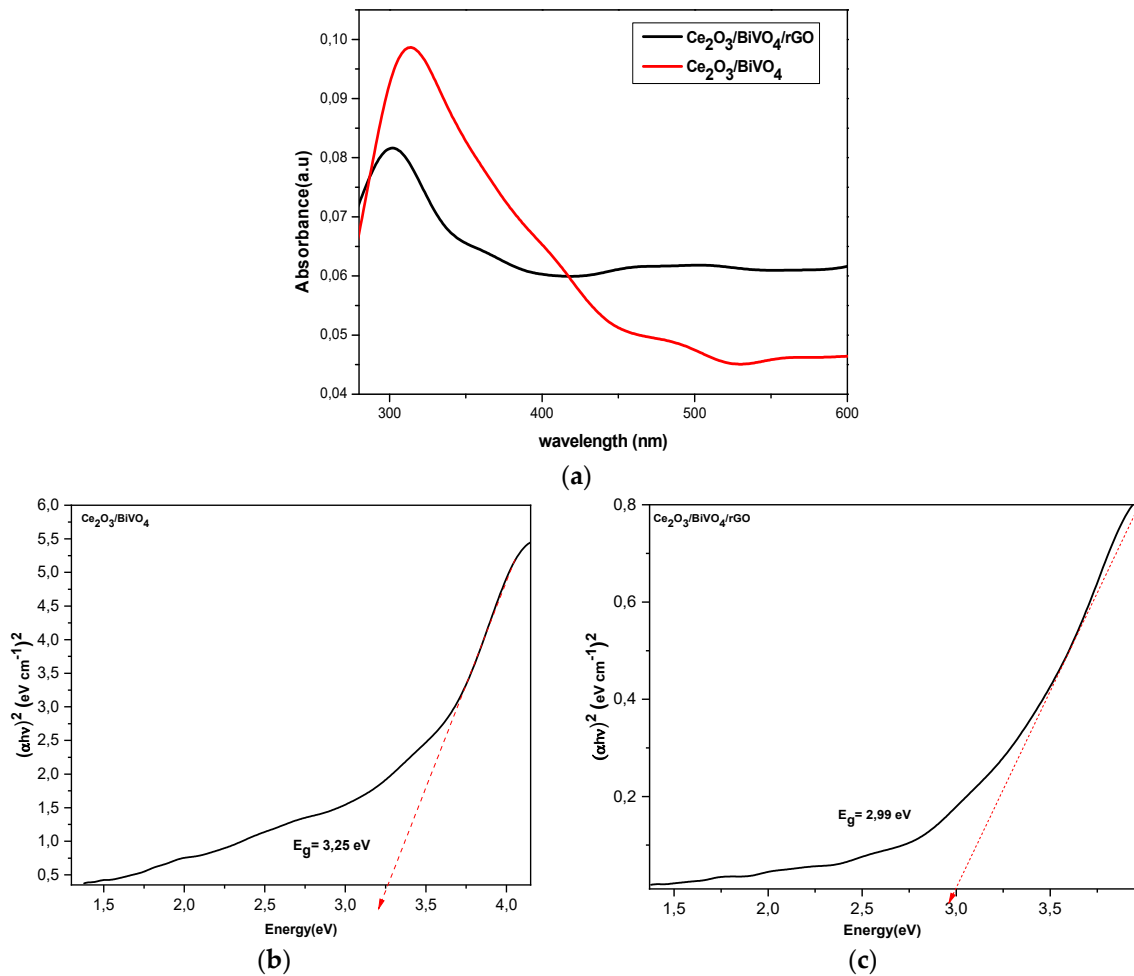


Figure 6. (a) UV-visible spectra of $\text{Ce}_2\text{O}_3/\text{BiVO}_4$ and $\text{Ce}_2\text{O}_3/\text{BiVO}_4/\text{rGO}$; Tauc plot for (b) $\text{Ce}_2\text{O}_3/\text{BiVO}_4$ and (c) $\text{Ce}_2\text{O}_3/\text{BiVO}_4/\text{rGO}$.

Based on the absorption spectra of the blank MO at different pH values (Figure 7a), the photocatalytic degradation study was conducted at pH 7. Figure 7b,c present the absorption spectra of methyl orange measured at 15 min intervals using $\text{Ce}_2\text{O}_3/\text{BiVO}_4$ and $\text{Ce}_2\text{O}_3/\text{BiVO}_4/\text{rGO}$, respectively, with 5 mg/L concentration of the catalyst. It could be observed that the methyl orange peak obviously decreased steadily under the visible light in the presence of the catalysts. Figure 7d presents a graph of the percentage degradation of the dye to the irradiation time in the presence and absence of the binary and ternary nanocomposites. After 120 min irradiation time, about 80% of MO was decomposed using $\text{Ce}_2\text{O}_3/\text{BiVO}_4/\text{rGO}$, and 70% was removed using $\text{Ce}_2\text{O}_3/\text{BiVO}_4$. However, the study conducted in the absence of the catalyst showed negligible degradation of the dye molecules even after 120 min of irradiation. In addition, Figure 7d showed that only about 15% and 18% of the dye was removed by the adsorption process using $\text{Ce}_2\text{O}_3/\text{BiVO}_4$ and $\text{Ce}_2\text{O}_3/\text{BiVO}_4/\text{rGO}$ within 15 min. The higher efficiency of the ternary nanocomposite ($\text{Ce}_2\text{O}_3/\text{BiVO}_4/\text{rGO}$) compared to the binary ($\text{Ce}_2\text{O}_3/\text{BiVO}_4$) could be ascribed to the formation of the heterojunction system coupled with the increase in the surface area as a result of the introduction of rGO, which implies that the composite with reduced graphene oxide is a better candidate for the photocatalytic degradation of MO.

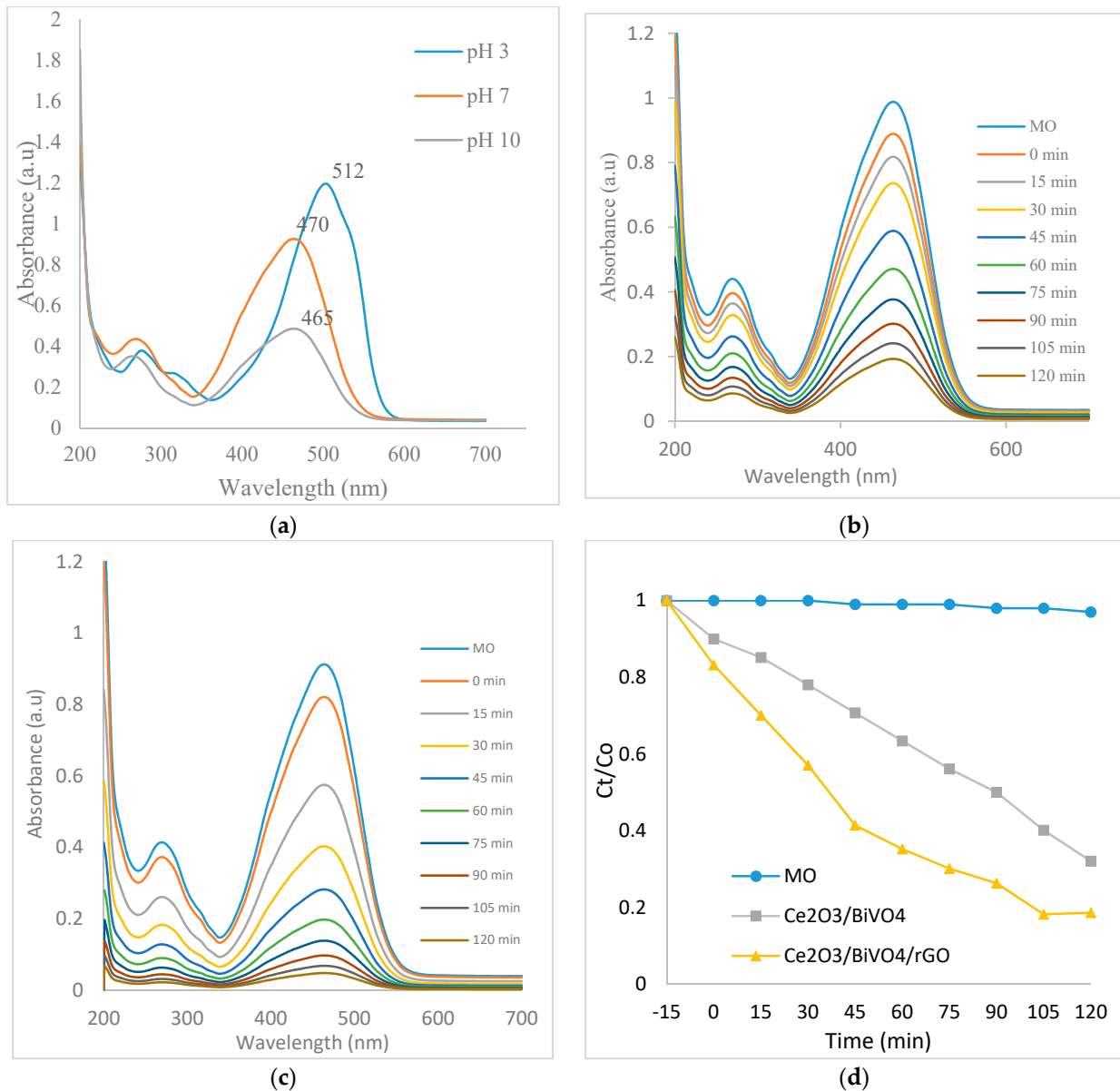


Figure 7. UV-visible absorption spectra of methyl orange (a); absorption spectra of the degradation of (MO) using $\text{Ce}_2\text{O}_3/\text{BiVO}_4$ (b), $\text{Ce}_2\text{O}_3/\text{BiVO}_4/\text{rGO}$ (c); and the degradation percentage of MO (d), using (5 mg/L catalyst, 1.0 g/L dye concentration, and initial pH 7.0 under visible light irradiation and in the dark).

3.5.1. Effect of Initial Dye Concentration

For both mechanistic purposes and from an application point of view, it is important to study the dependence of the photo-enhanced reaction process on the concentration of the substrate. The formation of hydroxyl radicals, a significant species in the degradation process, on the surface of the catalyst is the major determinant of the rate of degradation. Other related factors that are significant to the rate of degradation could be the adsorption of reactants on the catalyst surface as well as the side reaction rate of the hydroxyl radicals with other chemicals. Therefore, the factor k could be expressed as:

$$k = k_0 P_{\bullet\text{OH}} P_{\text{dye}} \tag{1}$$

where k is the overall rate constant, k_0 is the reaction rate constant, $P_{\bullet\text{OH}}$ is the probability of generation of $\bullet\text{OH}$ on the catalyst surface, and P_{dye} is the probability of $\bullet\text{OH}$ reacting with dye molecules. Since $P_{\bullet\text{OH}}$ and P_{dye} are implicitly dependent on the dye

concentration [51], it therefore implies that the rate of the dye degradation will decrease with an increase in the initial dye concentration. This is presumed to be due to the fact that the concentration of generated $\bullet\text{OH}$ on the surface of the photocatalyst will decrease as more dye ions cover the active sites of the photocatalyst. Another possible reason for the decrease in activity is as a result of the light-screening effect of the dye itself. A significant amount of light might be absorbed by the dye molecules rather than by the photocatalysts, at a high dye concentration, thereby resulting in a decrease in the formation of $\bullet\text{OH}$ as well as in the photocatalytic activity [52,53]. As shown in Figure 8a, the photocatalytic degradation efficiency of the MO was found to decrease at the initial MO concentrations of 5, 10, 15, 20, and 25 mg/L, which indicated that the overall rate constant k decreased with increase in the initial dye concentration.

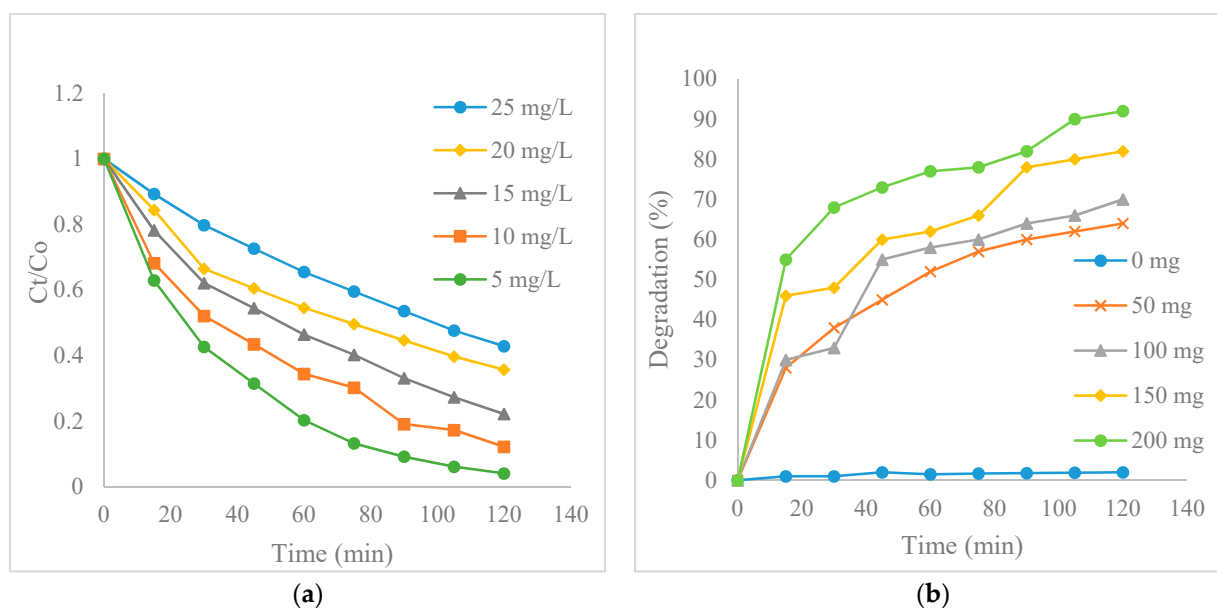


Figure 8. (a) Effect of initial dye concentration, and (b) Effect of catalysts loading on the photo degradation of MO (MO initial concentration: 10 mg/L, pH value (pH = 7)).

3.5.2. Effect of Catalysts Loading

Figure 8b presents the effect of catalysts loading on the degradation rate of MO. Only about 4.8% degradation was obtained in the absence of a catalyst after 120 min reaction. Degradation only commenced after the introduction of 50 mg/L of the catalyst and the rate increased with catalyst loading up to 200 mg/L. The catalyst displayed an abrupt increase in performance as the concentration was increased to 200 mg/L. The enhancement in the degradation efficiency could be attributed to the increased number of available adsorption and catalytic sites on the catalysts, as well as the reduced recombination of the electron-hole pairs due to the formation of heterojunction. However, it is important to indicate that a further increase in catalyst loading has been reported to cause light scattering and screening effects, which may probably cause a reduction in the specific activities of the catalysts [54]. In addition, it is possible for agglomeration and sedimentation of the catalysts particles to occur when high catalysts loading is used in the dye solution [54]. Under such circumstances, it is possible that part of the catalyst surface probably is now unavailable for both photon absorption and dye adsorption, thereby causing only less stimulation to the catalytic reaction. A degradation efficiency of 92.5% was obtained at 200 mg/L loading after 120 min at the initial MO concentration of 5 mg/L.

The long-term usage of the nanocomposite photocatalyst was evaluated by reusability and photo-stability studies, which were conducted by the repeated degradation study of the MO dye using a solution of 5 mg/L. Figure 9 presents the recyclability graph for four cycles, and the results clearly showed that despite the loss of a few amount

of the photocatalyst associated with the separation process, the photocatalyst could be effectively reused with just a slight loss in activity even after four consecutive cycles. Therefore, industrial application of this product is highly feasible owing to its stability and reusability properties.

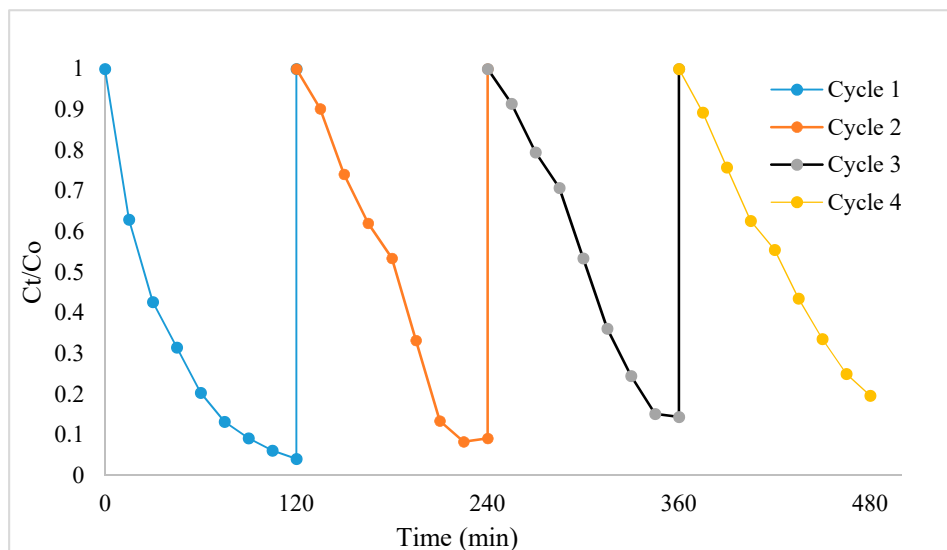


Figure 9. Reusability cycles of MO degradation using t $\text{Ce}_2\text{O}_3/\text{BiVO}_4/\text{rGO}$ nanocomposite and a solution of 5 mg/L dye.

4. Conclusions

The mixed metal oxide photocatalysts $\text{Ce}_2\text{O}_3/\text{BiVO}_4$ have been successfully incorporated into GO by the hydrothermal method. The particle size of the photocatalyst decreased upon GO addition with no changes in the crystal phase. The microscopic properties displayed a short rod-like morphology, which showed some elongation due to agglomeration. The composite exhibited enhanced photocatalytic activity under visible light irradiation, and the highest efficiency was found to be 90% within 2 h. The improved photocatalytic activity was attributed to the p–n heterojunction structure and the decreased recombination of the photogenerated excitations. The mechanism was based on the energy band positions of the nanoparticles within the composite. The activity of the catalyst could further be improved by reducing the dimension of the metal oxides. The photocatalyst composite is highly promising and competitive for dye removal application.

Author Contributions: Conceptualization, D.C.O.; methodology, B.M.P.; formal analysis, O.A.O.; investigation, B.M.P.; writing—original draft, D.C.O.; writing—review and editing, O.A.O. All authors have read and agreed to the published version of the manuscript.

Funding: BMP gratefully appreciate the National Research Foundation (NRF), South Africa for the award of bursary. All the authors acknowledge the North-West University, South Africa for financial assistance.

Data Availability Statement: All data have been reported in the manuscript and no other data is available elsewhere.

Acknowledgments: The authors gratefully acknowledge the North-West University and the National Research Foundation, South Africa for providing financial assistance.

Conflicts of Interest: The authors declare no conflict of interest.

References

1. Sivakumar, V.; Suresh, R.; Giribabu, K.; Narayanan, V. BiVO₄ nanoparticles: Preparation, characterization and photocatalytic activity. *Cogent Chem.* **2015**, *1*, 1074647. [CrossRef]
2. Xu, W.; Liu, Z.; Fang, J.; Zhou, G.; Hong, X.; Wu, S.; Zhu, X.; Chen, Y.; Cen, C. CTAB-Assisted Hydrothermal Synthesis of Bi₂Sn₂O₇ Photocatalyst and Its Highly Efficient Degradation of Organic Dye under Visible-Light Irradiation. *Int. J. Photoenergy* **2013**, *2013*, 394079. [CrossRef]
3. Lin, B.; Li, H.; An, H.; Hao, W.B.; Wei, J.J.; Dai, Y.Z.; Ma, C.S.; Yang, G.D. Preparation of 2D/2D g-C₃N₄ nanosheet@ZnIn₂S₄ nanoleaf heterojunctions with well-designed high-speed charge transfer nanochannels towards high efficiency photocatalytic hydrogen evolution. *Appl. Catal. B Environ.* **2018**, *220*, 542–552. [CrossRef]
4. Yang, K.; Li, X.; Yu, C.; Zeng, D.; Chen, F.; Zhang, K.; Huang, W.; Ji, H. Review on heterophase/homophase junctions for efficient photocatalysis: The case of phase transition construction. *Chin. J. Catal.* **2019**, *40*, 796–818. [CrossRef]
5. Kabachii, Y.A.; Golub, A.S.; Kochev, S.Y.; Lenenko, N.D.; Abramchuk, S.S.; Antipin, M.Y.; Valetsky, P.M.; Stein, B.D.; Mahmoud, W.E.; Al-Ghamdi, A.A.; et al. Multifunctional Nanohybrids by Self-Assembly of Monodisperse Iron Oxide Nanoparticles and Nanolamellar MoS₂ Plates. *Chem. Mater.* **2013**, *25*, 2434–2440. [CrossRef]
6. Yuzik-Klimova, E.Y.; Kuchkina, N.V.; Sorokina, S.A. Magnetically recoverable catalysts based on polyphenylenepyridyl dendrons and dendrimers. *RSC Adv.* **2014**, *4*, 23271–23280. [CrossRef]
7. Mahmoud, W.E. Solar blind avalanche photodetector based on the cation exchange growth of β-Ga₂O₃/SnO₂ bilayer heterostructure thin film. *Sol. Energy Mater. Sol. Cells* **2016**, *152*, 65–72. [CrossRef]
8. Al-Hazmi, F.S.; Al-Harbi, G.H.; Beall, G.W. Synthesis and structure of high quality graphene prepared via solvothermal exfoliation of intercalated graphite flakes. *Superlattices Microstruct.* **2015**, *86*, 270–274. [CrossRef]
9. Sitaaraman, S.R.; Shanmugapriyan, M.I.; Varunkumar, K. Synthesis of heterojunction tungsten oxide (WO₃) and Bismuth vanadate (BiVO₄) photoanodes by spin coating method for solar water splitting applications. *Mater. Today Proc.* **2020**. [CrossRef]
10. Lai, B.-R.; Lin, L.-Y.; Xiao, B.-C.; Chen, Y.-S. Facile synthesis of bismuth vanadate/bismuth oxide heterojunction for enhancing visible light-responsive photoelectrochemical performance. *J. Taiwan Inst. Chem. Eng.* **2019**, *100*, 178–185. [CrossRef]
11. Claudino, C.H.; Kuznetsova, M.; Rodrigues, B.S.; Chen, C.; Wang, Z.; Sardela, M.; Souza, J.S. Facile one-pot microwave-assisted synthesis of tungsten-doped BiVO₄/WO₃ heterojunctions with enhanced photocatalytic activity. *Mater. Res. Bull.* **2020**, *125*, 110783. [CrossRef]
12. Liu, Y.; Yuan, A.; Xiao, Y.; Yu, H.; Dong, X. Two-dimensional/two-dimensional Z-scheme photocatalyst of graphitic carbon nitride/bismuth vanadate for visible-light-driven photocatalytic synthesis of imines. *Ceram. Int.* **2020**, *46*, 16157–16165. [CrossRef]
13. Sun, M.; Yan, T.; Zhang, Y.; He, Y.; Shao, Y.; Wei, Q.; Du, B. Rod-like Bi₄O₇ decorated Bi₂O₂CO₃ plates: Facile synthesis, promoted charge separation, and highly efficient photocatalytic degradation of organic contaminants. *J. Colloid Interface Sci.* **2018**, *514*, 240–249. [CrossRef]
14. Sun, M.; Wang, Y.; Shao, Y.; He, Y.; Zeng, Q.; Liang, H.; Yan, T.; Du, B. Fabrication of a novel Z-scheme g-C₃N₄/Bi₄O₇ heterojunction photocatalyst with enhanced visible light-driven activity toward organic pollutants. *J. Colloid Interface Sci.* **2017**, *501*, 123–132. [CrossRef] [PubMed]
15. Ye, M.; Wei, W.; Zheng, L.; Liu, Y.; Wu, D.; Gu, X.; Wei, A. Enhanced visible light photoreduction of aqueous Cr(VI) by Ag/Bi₄O₇/g-C₃N₄ nanosheets ternary metal/non-metal Z-scheme heterojunction. *J. Hazard. Mater.* **2019**, *365*, 674–683. [CrossRef] [PubMed]
16. Jia, Y.; Li, S.; Ma, H.; Gao, J.; Zhu, G.; Zhang, F.; Park, J.Y.; Cha, S.; Bae, J.-S.; Liu, C. Oxygen vacancy rich Bi₂O₄-Bi₄O₇-BiO₂-x composites for UV-vis-NIR activated high efficient photocatalytic degradation of bisphenol A. *J. Hazard. Mater.* **2020**, *382*, 121121. [CrossRef]
17. Pujar, M.S.; Hunagund, S.M.; Barretto, D.A.; Desai, V.R.; Patil, S.; Vootla, S.K.; Sidarai, A.H. Synthesis of cerium-oxide NPs and their surface morphology effect on biological activities. *Bull. Mater. Sci.* **2020**, *43*. [CrossRef]
18. Nourmohammadi, E.; Khoshdel-Sarkarizi, H.; Nedaeinia, R.; Darroudi, M.; Kazemi Oskuee, R. Cerium oxide nanoparticles: A promising tool for the treatment of fibrosarcoma in-vivo. *Mater. Sci. Eng. C Mater. Biol. Appl.* **2020**, *109*, 110533. [CrossRef]
19. Albert, E.L.; Che Abdullah, C.A.; Shiroshaki, Y. Synthesis and characterization of graphene oxide functionalized with magnetic nanoparticle via simple emulsion method. *Results Phys.* **2018**, *11*, 944–950. [CrossRef]
20. Zhang, H.; Lv, X.; Li, Y.; Wang, Y.; Li, J. P25-graphene composite as a high performance photocatalyst. *ACS Nano* **2010**, *4*, 380–386. [CrossRef]
21. Pant, B.; Saud, P.S.; Park, M.; Park, S.-J.; Kim, H.-Y. General one-pot strategy to prepare Ag-TiO₂ decorated reduced graphene oxide nanocomposites for chemical and biological disinfectant. *J. Alloys Compd.* **2016**, *671*, 51–59. [CrossRef]
22. Pant, B.; Park, M.; Park, S.-J.; Kim, H.-Y. One-pot synthesis of CdS sensitized TiO₂ decorated reduced graphene oxide nanosheets for the hydrolysis of ammonia-borane and the effective removal of organic pollutant from water. *Ceram. Int.* **2016**, *42*, 15247–15252. [CrossRef]
23. Mahmoodi, N.M. Synthesis of core-shell magnetic adsorbent nanoparticle and selectivity analysis for binary system dye removal. *J. Ind. Eng. Chem.* **2014**, *20*, 2050–2058. [CrossRef]
24. Garg, N.; Bera, S.; Rastogi, L.; Ballal, A.; Balaramakrishna, M.V. Synthesis and characterization of L-asparagine stabilised gold nanoparticles: Catalyst for degradation of organic dyes. *Spectrochim. Acta Part A Mol. Biomol. Spectrosc.* **2020**, *232*, 118126. [CrossRef] [PubMed]

25. Zhu, D.; Zhou, Q. Action and mechanism of semiconductor photocatalysis on degradation of organic pollutants in water treatment: A review. *Environ. Nanotechnol. Monit. Manag.* **2019**, *12*, 100255. [[CrossRef](#)]
26. Mohammadi, P.; Sheibani, H. Green synthesis of Fe₃O₄@SiO₂-Ag magnetic nanocatalyst using safflower extract and its application as recoverable catalyst for reduction of dye pollutants in water. *Appl. Organomet. Chem.* **2018**, *32*, e4249. [[CrossRef](#)]
27. Lellis, B.; Fávoro-Polonio, C.Z.; Pamphile, J.A.; Polonio, J.C. Effects of textile dyes on health and the environment and bioremediation potential of living organisms. *Biotechnol. Res. Innov.* **2019**, *3*, 275–290. [[CrossRef](#)]
28. Hummers, W.S.; Offeman, R.E. Preparation of Graphitic Oxide. *J. Am. Chem. Soc.* **1958**, *80*, 1339. [[CrossRef](#)]
29. Cao, X.; Gu, Y.; Tian, H.; Fang, Y.; Johnson, D.; Ren, Z.; Chen, C.; Huang, Y. Microemulsion synthesis of ms/tz-BiVO₄ composites: The effect of pH on crystal structure and photocatalytic performance. *Ceram. Int.* **2020**, *46*, 20788–20797. [[CrossRef](#)]
30. Moreno-Román, E.J.; Cruz-López, A.; García-Gómez, C.; Zanella, R.; Suárez-Vázquez, S.I. Evaluation of the catalytic oxidation of soot by CeOX-LaMnO₃ at different O₂ pressures synthesized by ultrasonic-assisted hydrothermal method. *Environ. Sci. Pollut. Res. Int.* **2020**, *27*, 15475–15487. [[CrossRef](#)] [[PubMed](#)]
31. Gao, P.; Liu, J.; Sun, D.D.; Ng, W. Graphene oxide-CdS composite with high photocatalytic degradation and disinfection activities under visible light irradiation. *J. Hazard. Mater.* **2013**, *250–251*, 412–420. [[CrossRef](#)]
32. Yang, R.; He, J.; Niu, M.; Fan, Y.; Zhu, R. The photocatalytic activity of GO-modified BiVO₄ for the degradation of phenol under visible light irradiation. *Chem. Phys. Lett.* **2019**, *735*, 136770. [[CrossRef](#)]
33. Xiong, S.; Wu, T.; Fan, Z.; Zhao, D.; Du, M.; Xu, X. Preparation of a Leaf-Like BiVO₄ Reduced Graphene Oxide Composite and Its Photocatalytic Activity. *J. Nanomater.* **2017**, *2017*, 3475248. [[CrossRef](#)]
34. Dhandapani, P.; AlSalhi, M.S.; Karthick, R.; Chen, F.; Devanesan, S.; Kim, W.; Rajasekar, A.; Ahmed, M.; Aljaafreh, M.J.; Muhammad, A. Biological mediated synthesis of RGO-ZnO composites with enhanced photocatalytic and antibacterial activity. *J. Hazard. Mater.* **2020**, 124661. [[CrossRef](#)]
35. Ran, R.; McEvoy, J.G.; Zhang, Z. Synthesis and Optimization of Visible Light Active BiVO₄ Photocatalysts for the Degradation of RhB. *Int. J. Photoenergy* **2015**. [[CrossRef](#)]
36. Shandilya, P.; Mittal, D.; Soni, M.; Raizada, P.; Hosseini-Bandegharai, A.; Saini, A.K.; Singh, P. Fabrication of fluorine doped graphene and SmVO₄ based dispersed and adsorptive photocatalyst for abatement of phenolic compounds from water and bacterial disinfection. *J. Clean. Prod.* **2018**, *203*, 386–399. [[CrossRef](#)]
37. Pan, X.; Zhao, Y.; Liu, S.; Korzeniewski, C.L.; Wang, S.; Fan, Z. Comparing graphene-TiO₂; nanowire and graphene-TiO₂ nanoparticle composite photocatalysts. *ACS Appl. Mater. Interfaces* **2012**, *4*, 3944–3950. [[CrossRef](#)]
38. Qiu, J.; Zhang, P.; Ling, M.; Li, S.; Liu, P.; Zhao, H.; Zhang, S. Photocatalytic Synthesis of TiO₂ and Reduced Graphene Oxide Nanocomposite for Lithium Ion Battery. *ACS Appl. Mater. Interfaces* **2012**, *4*, 3636–3642. [[CrossRef](#)] [[PubMed](#)]
39. Khavar, A.H.; Moussavi, G.; Mahjou, A.R. The preparation of TiO₂@rGO nanocomposite efficiently activated with UVA/LED and H₂O₂ for high rate oxidation of acetaminophen: Catalyst characterization and acetaminophen degradation and mineralization. *Appl. Surf. Sci.* **2018**, *440*, 963–973. [[CrossRef](#)]
40. Bell, N.J.; Ng, Y.H.; Du, A.; Coster, H.; Smith, S.C.; Amal, R. Understanding the Enhancement in Photoelectrochemical Properties of Photocatalytically Prepared TiO₂-Reduced Graphene Oxide Composite. *J. Phys. Chem. C* **2011**, *115*, 6004–6009. [[CrossRef](#)]
41. Pant, B.; Pokharel, P.; Tiwari, A.P.; Saud, P.S.; Park, M.; Ghouri, Z.K.; Choi, S.; Park, S.-J.; Kim, H.-Y. Characterization and antibacterial properties of aminophenol grafted and Ag NPs decorated graphene nanocomposites. *Ceram. Int.* **2015**, *41*, 5656–5662. [[CrossRef](#)]
42. Chen, Y.; Liu, K. Fabrication of Ce/N co-doped TiO₂/diatomite granule catalyst and its improved visible-light-driven photoactivity. *J. Hazard. Mater.* **2017**, *324*, 139–150. [[CrossRef](#)]
43. Nogueira, A.E.; Silva, G.T.S.T.; Oliveira, J.A.; Lopes, O.F.; Torres, J.A.; Carmo, M.; Ribeiro, C. CuO Decoration Controls Nb₂O₅ Photocatalyst Selectivity in CO₂ Reduction. *ACS Appl. Energy Mater.* **2020**, *3*, 7629–7636. [[CrossRef](#)]
44. Torres-Luna, J.A.; Sanabria, N.R.; Carriazo, J.G. Powders of iron(III)-doped titanium dioxide obtained by direct way from a natural ilmenite. *Powder Technol.* **2016**, *302*, 254–260. [[CrossRef](#)]
45. Yan, W.; Hoekman, S.K.; Broch, A.; Coronella, C.J. Effect of Hydrothermal Carbonization Reaction Parameters on the properties of hydrochar and pellets. *Environ. Prog. Sustain. Energy* **2014**, *33*, 676–680. [[CrossRef](#)]
46. Wang, Y.; Wang, W.; Mao, H.; Lu, Y.; Lu, J.; Huang, J.; Ye, Z.; Lu, B. Electrostatic Self-Assembly of BiVO₄-Reduced Graphene Oxide Nanocomposites for Highly Efficient Visible Light Photocatalytic Activities. *ACS Appl. Mater. Interfaces* **2014**, *6*, 12698–12706. [[CrossRef](#)]
47. Zheng, Y.M.; Li, N.; De Zhang, W. Preparation of nanostructured microspheres of Zn-Mg-Al layered double hydroxides with high adsorption property. *Colloids Surf. A Phys. Eng. Asp.* **2012**, *415*, 195–201. [[CrossRef](#)]
48. Nguyen, C.H.; Fu, C.C.; Juang, R.S. Degradation of methylene blue and methyl orange by palladium-doped TiO₂ photocatalysis for water reuse: Efficiency and degradation pathways. *J. Clean. Prod.* **2018**, *202*, 413–427. [[CrossRef](#)]
49. Nezamzadeh-Ejhieh, A.; Karimi-Shamsabadi, M. Comparison of photocatalytic efficiency of supported CuO onto micro and nano particles of zeolite X in photodecolorization of Methylene blue and Methyl orange aqueous mixture. *Appl. Catal. A Gen.* **2014**, *477*, 83–92. [[CrossRef](#)]
50. Wei, T.Y.; Wan, C.C. Heterogeneous Photocatalytic Oxidation of Phenol with Titanium Dioxide Powders. *Ind. Eng. Chem. Res.* **1991**, *30*, 1293–1300. [[CrossRef](#)]

51. Saleh, R.; Djaja, N.F. UV light photocatalytic degradation of organic dyes with Fe-doped ZnO nanoparticles. *Superlattices Microstruct.* **2014**, *74*, 217–233. [[CrossRef](#)]
52. Zhang, X.; Zhang, X.; Fan, C.; Zong, Z.; Zhang, D.; Luo, Q.; Bi, C.; Fan, Y. A novel metal–organic frameworks assembled by one angular ligand and 5-aminoisophthalic acid: Synthesis, structure, electrochemical and photocatalytic properties. *Polyhedron* **2019**, *168*, 21–27. [[CrossRef](#)]
53. Rauf, M.A.; Meetani, M.A.; Hisaindee, S. An overview on the photocatalytic degradation of azo dyes in the presence of TiO₂ doped with selective transition metals. *Desalination* **2011**, *276*, 13–27. [[CrossRef](#)]
54. Sun, J.; Qiao, L.; Sun, S.; Wang, G. Photocatalytic degradation of Orange G on nitrogen-doped TiO₂ catalysts under visible light and sunlight irradiation. *J. Hazard. Mater.* **2008**, *155*, 312–319. [[CrossRef](#)] [[PubMed](#)]